Frequency-Domain Analysis of Single-Surface Multipactor Discharge With Single- and Dual-Tone RF Electric Fields

Asif Iqbal, *Student Member, IEEE*, Patrick Y. Wong, *Member, IEEE*, John P. Verboncoeur, *Fellow, IEEE*, and Peng Zhang, *Senior Member, IEEE*

***Abstract*— This article presents the frequency-domain analysis of multipactor discharge on a single dielectric surface. We employ the multiparticle Monte Carlo simulation model in one dimension with adaptive time steps to obtain the temporal profiles of the normal electric field, which is due to surface charging that corresponds to the multipactor strength, induced by single- or dual-tone radio frequency (RF) electric fields acting parallel to the surface. We apply a discrete Fourier transform (DFT) to obtain the amplitude spectrum of the normal electric fields. It is found that for the single-tone RF operation, the normal electric field consists of pronounced even harmonics of the driving RF frequency. The strength of a harmonic component in the normal electric field depends on its frequency and the incident RF amplitude. An empirical relation between the strength and frequency of the harmonics and the input RF amplitude has been proposed. For dual-tone RF operation, spectral peaks are observed in the amplitude spectrum of the normal electric field at various frequencies of intermodulation product of the RF carrier frequencies. Pronounced peaks are observed at the sum and difference frequencies of the carrier frequencies, at multiples of those frequencies, and at multiples of the carrier frequencies. Empirical relations between the heights of different spectral peaks and the input RF amplitudes have been proposed.**

***Index Terms*— Dual tone, frequency-domain analysis, intermodulation, Monte Carlo (MC), multipactor.**

I. Introduction

MULTIPACTOR [1]–[7] occurs when electrons accelerated by radio frequency (RF) fields are self-sustained via an electron avalanche caused by secondary electron emission from a metallic or dielectric surface. It may cause the breakdown of dielectric windows [8]–[10], erosion of metallic structures, melting of internal components, and perforation of vacuum walls [2]. For space-based communications, multipactor not only threatens the integrity of the microwave components but also degrades the signal quality, which has become a major concern [11]. An investigation of multipactor in high-power microwave (HPM) sources, RF accelerators [10], and space-based communication systems [12], [13] has been a major research focus over the years.

Extensive studies have been conducted on multipactor mitigation strategies including surface coating with low secondary electron yield (SEY) materials [14]–[17], using artificially roughened or porous surfaces with suppressed SEY [16]–[20], or by modifying the electric or magnetic fields for the single-surface [21]–[23], parallel-plate [24]–[28], microstrip [29], [30], and coaxial [31]–[33] geometries. The effects of space-charge [34]–[36], dual-tone [23], [24], [27], [37], and nonsinusoidal [38] transverse electric fields; external dc electric [5], [21] and magnetic fields [22], [39], [40]; oblique RF electric fields [22], [41]; and wave reflection [39], desorption, or background gases [5], [34] on multipactor discharge have been investigated with tools such as Monte Carlo (MC) particle simulations [4], particle-in-cell (PIC) simulations [42], [43], analytical calculations [4], statistical theory [44], and most recently with map-based theory [45] and chaos theory [46].

Studies have been conducted on the time-dependent physics of single-surface multipactor, revealing that the temporal profiles of the normal electric field and the SEY oscillate at twice of the RF frequency for single-tone operation [43] and at four times of the fundamental RF frequency for dual-tone operation with fundamental and second harmonic modes [37]. In addition to the temporal analysis, the frequency-domain analysis of multipactor discharge is also very important to understand the effect of multipactor on device operations. In this respect, Tang and Kudsia [47] investigated multipactor breakdown and passive intermodulation (PIM) in microwave components for satellite applications. Zhang *et al.* [48] investigated PIM in a parallel-plate transmission line (PPTL) caused by multipaction with 2-tone and 4-tone RF signals. Semenov *et al.* [49] proposed a simplified analytical model to predict the spectrum of electric current induced by the

Manuscript received November 15, 2019; revised February 8, 2020; accepted February 23, 2020. Date of publication March 19, 2020; date of current version June 10, 2020. The work was supported by the Air Force Office of Scientific Research (AFOSR) through the Multidisciplinary Research Program of the University Research Initiative (MURI) Grant No. FA9550-18-1-0062, and a Michigan State University (MSU) Foundation Strategic Partnership Grant. A. I. also acknowledges the support by the Michigan Institute for Plasma Science and Engineering (MIPSE) Graduate Fellowship. The review of this article was arranged by Senior Editor D. A. Shiffler. *(Corresponding author: Peng Zhang.)*

Asif Iqbal, Patrick Y. Wong, and Peng Zhang are with the Department of Electrical and Computer Engineering, Michigan State University, East Lansing, MI 48824 USA (e-mail: iqbalas3@egr.msu.edu; wongpat3@egr.msu.edu; pz@egr.msu.edu).

John P. Verboncoeur is with the Department of Computational Mathematics Science and Engineering, Michigan State University, East Lansing, MI 48824 USA, and also with the Department of Electrical and Computer Engineering, Michigan State University, East Lansing, MI 48824 USA (e-mail: johnv@egr.msu.edu).

Color versions of one or more of the figures in this article are available online at http://ieeexplore.ieee.org.

Digital Object Identifier 10.1109/TPS.2020.2978785

multipacting electrons between two parallel electrodes exposed to a single-tone RF electric field. However, the frequency-domain analysis of single-surface multipactor is rarely studied.

In this article, we examine multipactor discharge in the frequency domain on a single dielectric surface with single- and dual-tone RF signals. We employ the multiparticle MC simulation model [37] to obtain the temporal profiles of the normal electric field to the surface that corresponds to the multipactor strength in the system. We perform a discrete Fourier transform (DFT) on the temporal profiles and obtain the amplitude spectrum of the normal electric fields in the ac saturation state. For single-tone RF electric fields, the spectral peaks are observed at the even harmonics of the fundamental RF frequency. We find that the heights of the spectral peaks depend on their frequencies and also on the input RF amplitude. For dual-tone RF electric fields, spectral peaks are observed at various frequencies of intermodulation products in the amplitude spectrum of the normal electric field. We propose the empirical relations between the heights of the spectral peaks and the input RF carrier amplitude. The temporal profiles of the normal electric fields obtained from MC simulation and from the proposed empirical scalings are in excellent agreement for both single- and dual-frequency RF electric fields.

II. Electron Dynamics and MC Model

The multipactor electrons are subjected to forces imposed by the normal electric field E_x originating from the residual charge on the dielectric acting along the x-direction and the RF electric field $E_y = [E_{\rm rf}\sin(\omega t+\theta)+\beta E_{\rm rf}\sin(n(\omega t+\theta)+\gamma)]$ acting along the y-direction (Fig. 1). Here, $E_{\rm rf}$ is the peak electric field strength, ω is the angular frequency, and θ is the initial phase of the electric field of the fundamental carrier mode. β is the field strength of the second carrier mode relative to the fundamental mode, n is the ratio of the frequencies of the two carrier modes, and γ is the relative phase of the second carrier mode. Here, n needs not be an integer. Except for the time-varying strength of E_x, the possible space-charge effects due to multipactor electrons [22], [34], [42], [50] are not considered. As shown in Fig. 1, the flight trajectory of a multipactor electron is governed by the force law

$$m\frac{\partial \vec{v}}{\partial t} = -|e|[\vec{E}_{\rm rf}\sin(\omega t+\theta)+\beta\vec{E}_{\rm rf}\sin(n(\omega t+\theta)+\gamma)+\vec{E}_x]. \tag{1}$$

From this, we obtain

$$v_x = -\frac{|e|}{m}E_x t + v_0\sin\phi \tag{2a}$$

$$v_y = \frac{|e|}{m\omega}E_{\rm rf}\left\{\cos(\omega t+\theta)-\cos\theta + \frac{\beta}{n}\left[\cos(n(\omega t+\theta)+\gamma)-\cos(n\theta+\gamma)\right]\right\} + v_0\cos\phi \tag{2b}$$

where the last terms account for the emission velocity at $t = 0$. From (2), we obtain the instantaneous position of a multipactor electron as

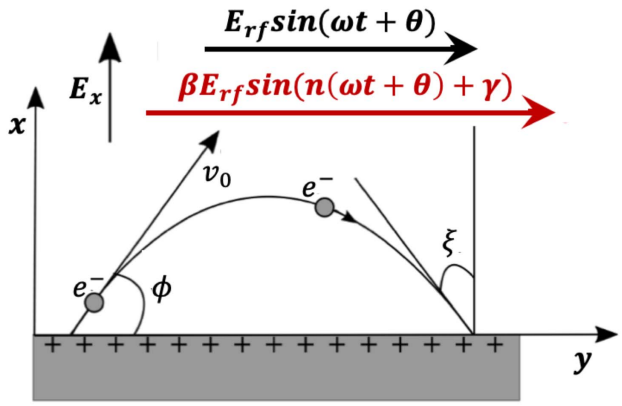

Fig. 1. Schematic of the single-surface multipactor discharge in a normal electric field and a dual-tone parallel RF field.

$$x = -\frac{|e|}{2m}E_x t^2 + v_0 t\sin\phi + x_0 \tag{3a}$$

$$y = \frac{|e|}{m\omega}E_{\rm rf}\left\{\frac{1}{\omega}\sin(\omega t+\theta)-t\cos\theta + \frac{\beta}{n}\left[\frac{1}{n\omega}\sin(n(\omega t+\theta)+\gamma)-t\cos(n\theta+\gamma)\right]\right\} + v_0 t\cos\phi + y_0 \tag{3b}$$

where x_0 and y_0 account for the initial position of the particles at $t = 0$. The transit time τ of an electron in flight before impacting the dielectric surface is calculated by solving (3a) for $x = 0$. It is noteworthy that the solutions to (1) given in (2a), (2b), (3a), and (3b) apply only during the intervals between any two consecutive impacts from the entire ensemble of particles on the surface, during which the normal electric field E_x remains constant. Note also that E_x changes upon the impact of any particle.

The SEY, δ, defined as the average number of secondary electrons produced by the impact of each primary electron upon the surface, is a function of the impact energy of the primary electron, E_i, and the angle to the normal, ξ, at which it strikes the surface [51]. It also depends on material properties translating into two parameters: the maximum yield, $\delta_{\max}$, and the energy at which it occurs, $E_{\max}$. We specify these parameters for the simulation as discussed in [23] and adopt the following Vaughan's empirical formula [51], [52] to estimate the SEY:

$$\frac{\delta(\xi)}{\delta_{\max}(\xi)} = (we^{1-w})^k, \quad \text{for } w \le 3.6 \tag{4a}$$

$$\frac{\delta(\xi)}{\delta_{\max}(\xi)} = 1.125/w^{0.35}, \quad \text{for } w > 3.6 \tag{4b}$$

where $w = E_i/E_{\max}$, $k = 0.56$ for $w < 1$, $k = 0.25$ for $1 \le w \le 3.6$, $E_{\max} = E_{\max 0}(1+k_{sE}\xi^2/2\pi)$, and $\delta_{\max} = \delta_{\max 0}(1+k_{s\delta}\xi^2/2\pi)$, where k_{sE} and $k_{s\delta}$ are surface smoothness factors, both of which are set to 1 in the simulation. Two values of impact energy, termed the first and second crossover points, E_1 and E_2, respectively, result in a yield of 1, with $\delta > 1$ in between.

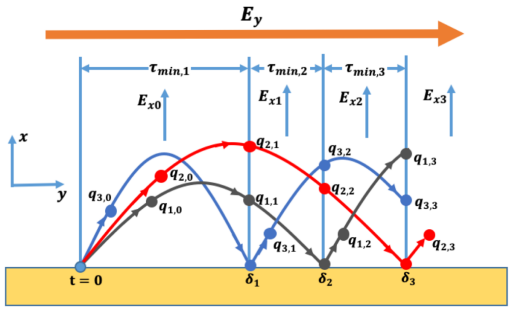

	Particle #1	Particle #2	Particle #3
Iteration #1	$q_{1,0}$	$q_{2,0}$	$q_{3,0}$
Iteration #2	$q_{1,1}$=$q_{1,0}$	$q_{2,1} = q_{2,0}$	$q_{3,1} = \delta_1 q_{3,0}$
Iteration #3	$q_{1,2} = \delta_2 q_{1,1}$	$q_{2,2} = q_{2,1}$	$q_{3,2} = q_{3,1}$
Iteration #4	$q_{1,3} = q_{1,2}$	$q_{2,3} = \delta_3 q_{2,2}$	$q_{3,3} = q_{3,2}$

Fig. 2. Schematic of the multiparticle MC modeling of the single-surface multipactor discharge: multiple macroparticles are in flight, and each iteration traces one impact of a macroparticle onto the surface; charge, q_i, and mass, m_i, of only the incident macroparticle hitting the surface are updated after each iteration. Total surface charge, N_s, and the normal electric field, E_x, are calculated as described in [37]. Reproduced from [37], with the permission of AIP Publishing.

Following the algorithm described in [37], we start the simulation with $N = 100$ weighted macroparticles emitted at time $t = 0$ from the initial position $x = 0$ and $y = 0$ of a surface (Fig. 2). An initial electric field E_{x0} ($E_{x0} \sim E_{\mathrm{rf}0}/30$) is assigned normal to the surface, and the initial surface charge is calculated as $N_s = 2AE_{x0}\epsilon_0/|e|$, where A is the area of the dielectric surface. The same amount of negative charge is evenly distributed to the $N = 100$ initial macroparticles. We follow the trajectory of these macroparticles over a large number of impacts ($N_{\mathrm{impact}} = 8 \times 10^4$) in an MC simulation [4], [5]. Each time a macroparticle leaves the surface, we assign it a random initial energy $E_0 = (1/2)\,mv_0^2$ and angle ϕ according to the following distributions [4]:

$$f(E_0) = \frac{E_0}{E_{0m}^2} e^{-\left(\frac{E_0}{E_{0m}}\right)} \tag{5a}$$

$$g(\phi) = \frac{1}{2}\sin\phi \tag{5b}$$

where E_{0m} is the peak of the distribution of emission energies, on the order of the work function, i.e., a few electron volts [2]–[4]. The expected value of E_0 is $2E_{0m}$ and $\int g(\phi)\,d\phi = 1$ over $0 < \phi < \pi$. Substituting these random values of initial velocities and angles into (2) and (3), we obtain the transit times of each macroparticle before impacting the surface and find the minimum of these transit times, $\tau_{\min}$, which identifies the macroparticle that impacts the surface next. We calculate this macroparticle's impact energy, E_i, and impact angle, ξ, and hence, the SEY, δ, of the impact from (4). We use this value of the yield to adjust the charge and mass on the impacting macroparticle and then emit it again with a random velocity and emission angle. The charges and masses of all the other macroparticles in flight are unchanged by this impact, and we record their instantaneous velocities and positions at the time of the impact to use in the next iteration. Total surface charge and normal electric field values are also updated accordingly at the time of each impact [37]. The initial RF phase of the fundamental carrier in our simulation is assigned as $\theta = 0$, and then, it is calculated self-consistently ($\theta_{i+1} = \theta_i + \omega\tau_{\min}$) at the beginning of each iteration. For all the cases, in this article, the relative phase between the two tones is assigned as $\gamma = 0$. The temporal profiles of the surface charge N_s and the normal electric field to the dielectric surface E_x are obtained by converting the iteration number into the scale of time using the transit times $\tau_{\min}$ for each iteration. E_x obtained at this stage is on a nonuniform grid in time. We divide the time scale in uniform bins and compute the average E_x in each of those bins. We then employ a fast Fourier transform (FFT) algorithm of MATLAB to obtain the DFT of the temporal profiles of E_x.

It is important to note that the multiparticle MC and PIC results from [43], where each impact produces a "spray" of secondary electrons, match almost exactly with each other in the saturation regime. This confirms that it is adequate to emit just one particle at each impact site in the multiparticle MC [37]. Furthermore, it indicates that the space-charge effect (included in the PIC simulation but missing in MC) has little effect on the multipactor development and, therefore, the harmonic contents of E_x in the chosen input parameters.

III. Results

The previous studies conducted by Kim and Verboncoeur [43] and Iqbal *et al.* [37] showed that for a single-tone RF electric field [Fig. 3(a)], the temporal profile of the normal electric field E_x oscillates at twice the RF frequency in the ac saturation state [Fig. 3(b)]. It is also understood [3], [23], [37] that the ac saturation for a given RF amplitude occurs at the lower multipactor susceptibility boundary of Fig. 3(c). For instance, for the RF amplitude $E_{\mathrm{rf}0} = 3$ MV/m of Fig. 3(a), the ac saturation occurs at point "A" of Fig. 3(c), where the time averaged normal electric field is $E_x = 0.93$ MV/m. It is evident from Fig. 3(b) that the oscillation in the normal electric field profile is not purely sinusoidal and has multiple frequency components. We employ DFT to obtain the amplitude spectrum of the normal electric field E_x and observe its frequency components for different RF amplitudes and frequencies.

Figure 4 shows the amplitude spectrum of the normal electric field E_x for three different cases of a single-tone RF field. The RF amplitude is kept fixed at $E_{\mathrm{rf}0} = 3$ MV/m, and the RF frequency is varied as $f_{\mathrm{rf}} = 1, 1.5$, and 2 GHz from Fig. 4(a)–(c), respectively.

As shown in Fig. 4, the peaks in the amplitude spectrum of E_x appear at even harmonics of the RF frequency, $2lf_{\mathrm{rf}}$, where l is a positive integer. We also observe that the heights of the spectral peaks gradually decrease with the increase of their frequencies. However, the heights of the spectral peaks are almost independent of the RF frequency. It is noteworthy that the normal surface charging field E_x consists of even harmonics of the RF frequency only. This is expected since surface charging due to multipactor discharge from a single dielectric surface is independent of the direction (i.e., either positive or negative) of the parallel RF electric field E_{rf}, and the normal surface charging field E_x must be symmetric in the positive and negative half cycles of E_{rf}.

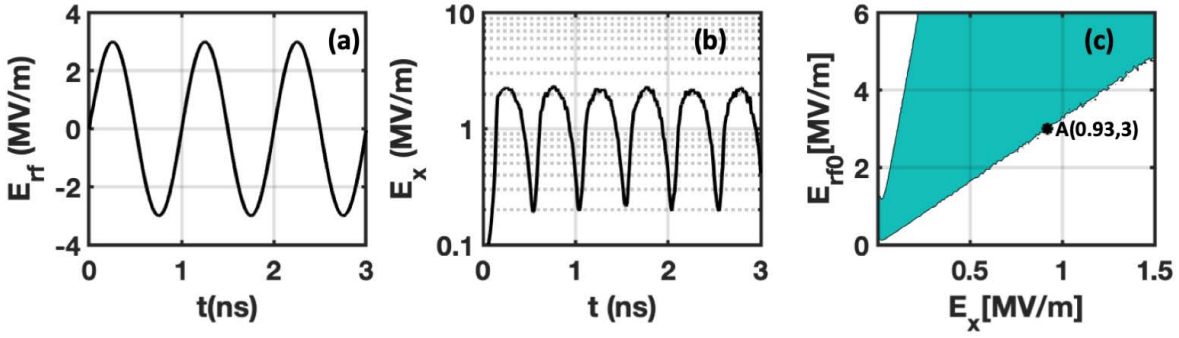

Fig. 3. (a) Temporal profile of the RF field with a frequency $f_{\rm rf} = 1$ GHz and amplitude $E_{\rm rf0} = 3$ MV/m. (b) Temporal profile of the normal electric field E_x in the ac saturation state obtained from the MC simulation. (c) Multipactor susceptibility boundaries (blue regions are subjected to multipactor susceptibility) in the $(E_x, E_{\rm rf0})$ plane from MC simulation with single-tone RF field. Here, the maximum SEY, $\delta_{\rm max0} = 3$, occurring at impact energy $E_{\rm max0} = 420$ eV, and $E_{m0}/E_{\rm max0} = 0.005$, where $2E_{m0}$ is the average emission energy of secondary electrons. In the calculation of (c), E_x is kept as a constant for each case, and the susceptibility is recorded when $\delta_{\rm avg} > 1$.

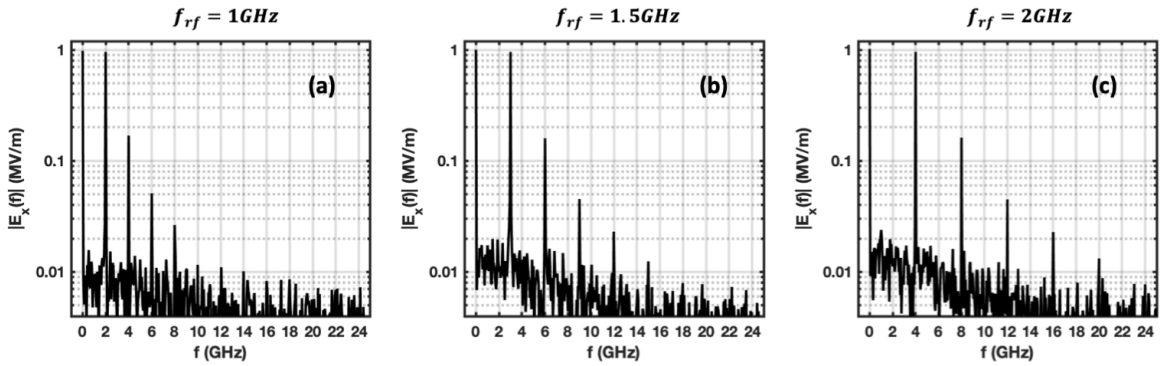

Fig. 4. Amplitude spectrum of the normal electric field in the ac saturation state induced by a single-tone RF field with amplitude, $E_{\rm rf0} = 3$ MV/m, and frequencies, $f_{\rm rf} =$ (a)1 GHz, (b) 1.5 GHz, and (c) 2 GHz. Pronounced spectral peaks are observed at even harmonics of the RF frequency in each case. The heights of the spectral peaks are independent of the RF frequency.

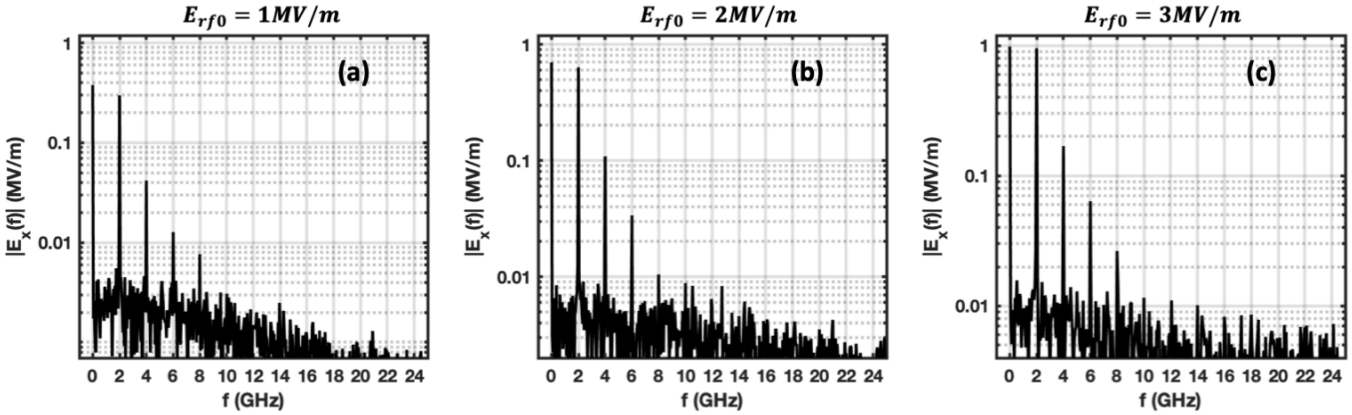

Fig. 5. Amplitude spectrum of the normal electric field in the ac saturation state induced by a single-tone RF field with RF frequency, $f_{\rm rf} = 1$ GHz, and RF amplitudes, $E_{\rm rf0} =$ (a) 1 MV/m, (b) 2 MV/m, and (c) 3 MV/m. Pronounced spectral peaks are observed at even harmonics of the RF frequency in each case. The heights of the spectral peaks increase linearly with the increase of the RF amplitude.

In Fig. 5, we plot the amplitude spectrum of E_x for RF amplitudes $E_{\rm rf0} = 1$, 2, and 3 MV/m while the RF frequency is kept fixed at $f_{\rm rf} = 1$ GHz. It is clear from these plots that the heights of the spectral peaks at even harmonics increase as the RF amplitude increases. We can express the relation between the heights of the spectral peaks, E_{xl}, at even harmonic frequencies of the RF frequency, $f = 2lf_{\rm rf}$, and the RF amplitude, $E_{\rm rf0}$, with the following linear equation:

$$E_{xl}(\text{MV/m}) = A_l E_{\rm rf0}(\text{MV/m}) + B_l. \tag{6}$$

By curve fitting, we obtain the following empirical formula for the coefficients A_l and B_l:

$$A_l = a(2l)^b \tag{7a}$$

$$B_l = c(2l) + d. \tag{7b}$$

For the DFT results in Figs. 4 and 5, we find $a = 1.709$, $b = -2.379$, $c = 0.004$, and $d = -0.036$. The temporal profiles of the normal electric field can be expressed in terms of the

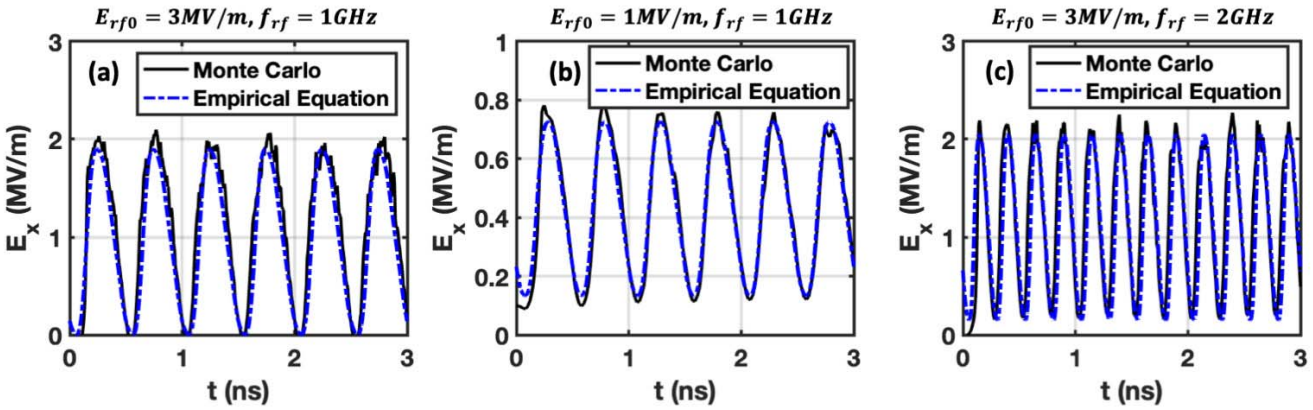

Fig. 6. Temporal profiles of the normal electric field E_x in the ac saturation state obtained from the MC simulation (black solid lines) and the empirical (8) (blue dashed lines) for single-tone RF fields with (a) RF amplitude $E_{\mathrm{rf0}} = 3$ MV/m and RF frequency $f_{\mathrm{rf}} = 1$ GHz, (b) $E_{\mathrm{rf0}} = 1$ MV/m and $f_{\mathrm{rf}} = 1$ GHz, and (c) $E_{\mathrm{rf0}} = 3$ MV/m and $f_{\mathrm{rf}} = 2$ GHz. The time averaged saturation values used in these cases are $E_{x,\mathrm{avg}} = 0.93, 0.42$, and 1.03 MV/m, respectively.

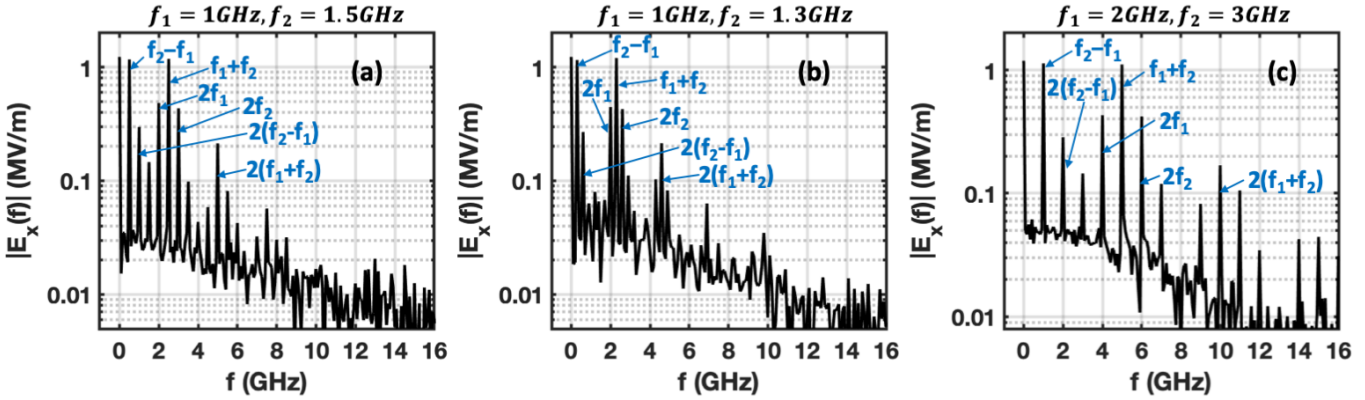

Fig. 7. Amplitude spectrum of the normal electric field in the ac saturation state induced by a dual-tone RF field with individual carrier amplitude, $E_{\mathrm{rf0}} = 3$ MV/m [with $\beta = 1$ in (1)], and carrier frequencies, (a) $f_1 = 1$ GHz, $f_2 = 1.5$ GHz, (b) $f_1 = 1$ GHz, $f_2 = 1.3$ GHz, and (c) $f_1 = 2$ GHz, $f_2 = 3$ GHz. Pronounced spectral peaks are observed at frequencies $(f_2 \pm f_1)$, $2f_{1,2}$, and $2(f_2 \pm f_1)$.

DFT peaks as follows:

$$E_x \cong E_{x,\mathrm{avg}} + \sum_{l=1}^{4} E_{xl} \sin(2l\omega_0 t) \tag{8}$$

where $E_{x,\mathrm{avg}}$ is the time averaged value of the normal electric field in the ac saturation state, which is the peak observed at frequency $f = 0$ in the amplitude spectrum of E_x, and $\omega_0 = 2\pi f_{\mathrm{rf}}$ is the angular frequency of the RF field. It is noteworthy that, for a given E_{rf0}, the value of $E_{x,\mathrm{avg}}$ can also be interpolated at point "A" from the lower susceptibility boundary of the susceptibility diagram of Fig. 3(c).

In Fig. 6, we have the temporal profiles of the normal electric fields obtained from (8) (blue dashed lines) and from the MC simulation (black solid lines), showing very good agreement. The differences are due to the fact that, in (8), we only included the first four even harmonics which were the most pronounced in the amplitude spectrums. The higher harmonics of E_x could not be recovered with confidence due to the background noises of the DFT. Here, it is important to note that even though the coefficients used in (6) are obtained by fitting the data in Figs. 4 and 5, they remain applicable to new cases in Fig. 6.

We extend the analysis to multipactor due to dual-tone RF fields. Figure 7 shows the amplitude spectrum of the normal electric field E_x for three cases of a dual-tone RF field. The individual RF amplitude is kept fixed at $E_{\mathrm{rf0}} = 3$ MV/m [with $\beta = 1$ in (1)] for all three cases. The carrier frequencies are varied as $f_1 = 1$ GHz and $f_2 = 1.5$ GHz [Fig. 7(a)], $f_1 = 1$ GHz and $f_2 = 1.3$ GHz [Fig. 7(b)], and $f_1 = 2$ GHz and $f_2 = 3$ GHz [Fig. 7(c)], corresponding to $n = f_2/f_1 = 1.5$, 1.3, and 1.5 in (1), respectively. We observe spectral peaks at various frequencies of intermodulation products in the amplitude spectrum of E_x. The pronounced peaks are observed at the sum and difference frequencies of the carrier frequencies, at multiples of those frequencies, and at multiples of the individual carrier frequencies. We list the frequencies of the most pronounced peaks shown in Fig. 7(a)–(c) and Table I.

We observe from Fig. 7 that the heights of the different intermodulation peaks, $f_2 \pm f_1$, $2f_{1,2}$, and $2(f_2 \pm f_1)$, remain unchanged with the change of the carrier frequencies. For all three cases, the two strongest peaks have equal spectral heights and appear at the sum and difference frequencies of the

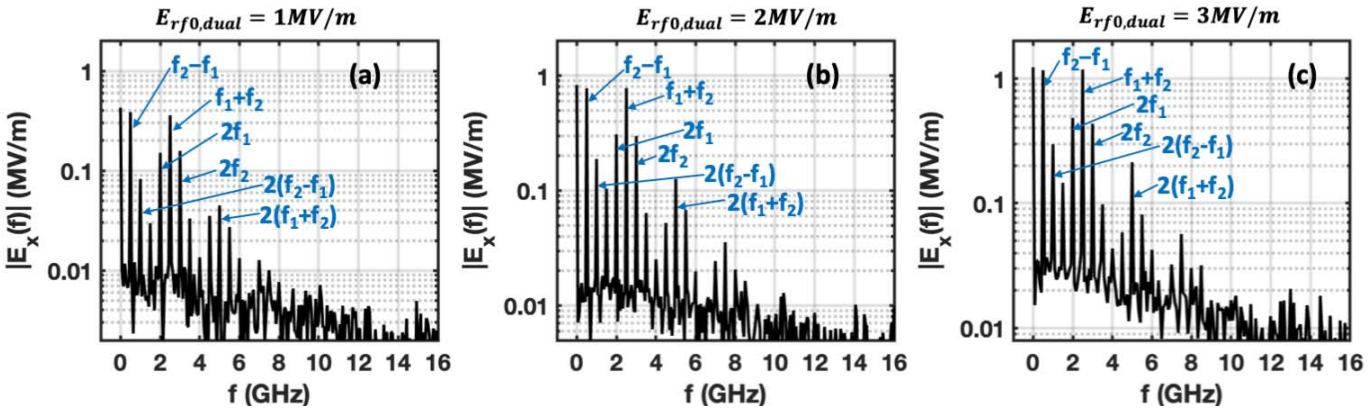

Fig. 8. Amplitude spectrum of the normal electric field in the ac saturation state induced by a dual-tone RF field with carrier frequencies $f_1 = 1$ GHz, $f_2 = 1.5$ GHz [i.e., $n = 1.5$ in (1)] and equal RF amplitudes [$\beta = 1$ in (1)] for the two carriers, $E_{\mathrm{rf0,dual}} =$ (a) 1 MV/m, (b) 2 MV/m, and (c) 3 MV/m. Pronounced spectral peaks are observed at frequencies $(f_2 \pm f_1), 2f_{1,2}$, and $2(f_2 \pm f_1)$. The heights of the spectral peaks increase with the RF amplitude.

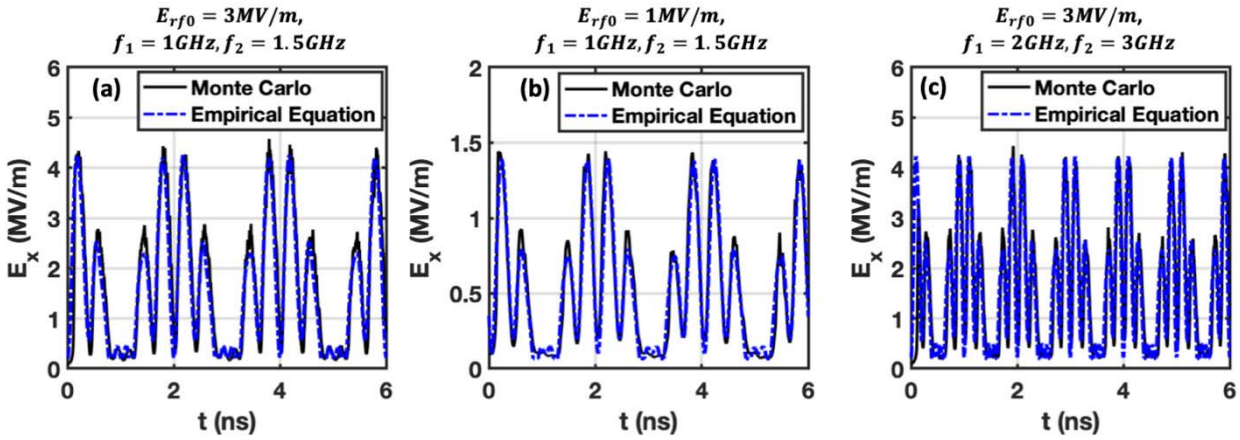

Fig. 9. Temporal profiles of the normal electric field E_x in the ac saturation state obtained from the MC simulation (black solid lines) and empirical (9) (blue dashed lines) for dual-frequency RF fields with (a) $E_{\mathrm{rf0,dual}} = 3$ MV/m, $f_1 = 1$ GHz, $f_2 = 1.5$ GHz, (b) $E_{\mathrm{rf0,dual}} = 1$ MV/m, $f_1 = 1$ GHz, $f_2 = 1.5$GHz, and (c) $E_{\mathrm{rf0,dual}} = 3$ MV/m, $f_1 = 2$ GHz, $f_2 = 3$ GHz. The time-averaged saturation values used in these cases are $E_{\mathrm{x,avg}} = 1.3, 0.52$, and 1.3 MV/m, respectively.

TABLE I

FREQUENCIES OF PROMINENT SPECTRAL PEAKS IN FIG. 7. ALL THE FREQUENCIES ARE IN GHz

RF frequencies		Frequencies of the strongest peaks		Frequencies of the 2nd strongest peaks		Frequencies of the next two strongest peaks	
f_1	f_2	$f_2 - f_1$	$f_1 + f_2$	$2f_1$	$2f_2$	$2(f_2 - f_1)$	$2(f_1 + f_2)$
1	1.5	0.5	2.5	2	3	1	5
1	1.3	0.3	2.3	2	2.6	0.6	4.6
2	3	1	5	4	6	2	10

carrier frequencies, $f_2 \pm f_1$. The two second strongest peaks with equal heights appear at twice the carrier frequencies, $2f_{1,2}$. The third and fourth strongest peaks appear at twice the difference, $2(f_2 - f_1)$, and twice the sum, $2(f_2 + f_1)$, of the carrier frequencies, respectively. A number of weaker peaks are also observed at various intermodulation products of the carrier frequencies. For instance, we find weaker peaks at the frequencies $3f_1 - f_2 = 1.5$ GHz, $3f_2 - f_1 = 3.5$ GHz, $3f_1 + f_2 = 3f_2 = 4.5$ GHz, $f_1 + 3f_2 = 5.5$ GHz, $3f_1 + 2f_2 = 6$ GHz, and $3(f_1 + f_2) = 7.5$ GHz in Fig. 7(a), at frequencies $3f_2 - f_1 = 2.9$ GHz, $3f_1 + f_2 = 4.3$ GHz, $f_1 + 3f_2 = 4.9$ GHz, and $3(f_1 + f_2) = 6.9$ GHz in Fig. 7(b), and at frequencies $3f_1 - f_2 = 3$ GHz, $3f_2 - f_1 = 7$ GHz, $3f_2 = 9$ GHz, $f_1 + 3f_2 = 11$ GHz, $3f_1 + 2f_2 = 12$ GHz, $f_1 + 4f_2 = 14$ GHz, and $3(f_1 + f_2) = 15$ GHz in Fig. 7(c).

In Fig. 8, we plot the amplitude spectrum of the normal electric field by a dual-frequency RF field with carrier frequencies,

TABLE II

EMPIRICAL VALUES OF COEFFICIENTS A_l AND B_l AT FREQUENCIES OF INTERMODULATION PRODUCTS WITH THE STRONGEST PEAKS

l	Frequency (f_l^{IM})	Coefficient A_l	Coefficient B_l
1	$f_2 - f_1$	0.4005	−0.02547
2	$f_1 + f_2$		
3	$2f_1$	0.1518	−0.001782
4	$2f_2$		
5	$2(f_2 - f_1)$	0.1073	−0.02528
6	$2(f_1 + f_2)$	0.08427	−0.04026

$f_1 = 1$ GHz and $f_2 = 1.5$ GHz, and equal amplitudes for the two carriers [i.e., $n = 1.5$ and $\beta = 1$ in (1)], for $E_{\text{rf0}} = 1$, 2, and 3 MV/m. It is clear that the heights of the spectral peaks increase as the RF amplitude increases. The relation between the spectral peak heights at different frequencies of intermodulation products and the RF amplitude can still be fitted with the linear relation (6), with the coefficients A_l and B_l shown in Table II.

For dual-frequency operation, the temporal profiles of the normal electric field are approximated as follows:

$$E_x \cong E_{x,\text{avg}} + \sum_{l=1}^{6} E_{xl} \sin\left(2\pi f_l^{IM} t\right) \tag{9}$$

where $E_{x,\text{avg}}$ is the time averaged value of the normal electric field in the ac saturation state, which is the peak observed at frequency $f = 0$ in the amplitude spectrum of E_x, and f_l^{IM} denotes the frequencies of intermodulation products, as shown in Figs. 7 and 8. Figure 9 shows the temporal profiles of E_x obtained from (6) and (9) with coefficients in Table II (blue dashed lines) and from the MC simulation (black solid lines), showing very good agreement. The differences are due to the fact that only the first six strongest frequency peaks are included in (9). More frequency components can be added to (9) to give better predictions.

IV. CONCLUSION

This article presents a frequency-domain investigation of multipactor discharge in single dielectric surfaces exposed to single- and dual-tone RF electric fields. The study was carried out using the multiparticle MC simulation model in one dimension with adaptive time steps. It is observed that the amplitude spectrum of the normal electric field induced by a single-tone RF field consists of pronounced peaks at even harmonics of the driving RF frequency. For dual-tone RF operation, the normal electric field in the ac saturation state consists of frequency components at various intermodulation products. We identify the frequencies of the pronounced spectral peaks and propose the empirical relations between the height of the strongest peaks and the input RF amplitude.

Further studies may include investigation of how these frequency components of the normal electric field can be useful in applications, such as high harmonic generation [53], assess their impacts on the quality of the transmitted RF signals [11], and extend the frequency-domain analysis for multipactor excited under multifrequency operation.

REFERENCES

[1] P. T. Farnsworth, "Television by electron image scanning," *J. Franklin Inst.*, vol. 218, no. 4, pp. 411–444, Oct. 1934.

[2] J. R. M. Vaughan, "Multipactor," *IEEE Trans. Electron Devices*, vol. 35, no. 7, pp. 1172–1180, Jul. 1988.

[3] R. A. Kishek and Y. Y. Lau, "Multipactor discharge on a dielectric," *Phys. Rev. Lett.*, vol. 80, no. 1, pp. 193–196, Jan. 1998.

[4] R. A. Kishek, Y. Y. Lau, L. K. Ang, A. Valfells, and R. M. Gilgenbach, "Multipactor discharge on metals and dielectrics: Historical review and recent theories," *Phys. Plasmas*, vol. 5, no. 5, pp. 2120–2126, May 1998, doi: 10.1063/1.872883.

[5] P. Zhang, Y. Y. Lau, M. Franzi, and R. M. Gilgenbach, "Multipactor susceptibility on a dielectric with a bias DC electric field and a background gas," *Phys. Plasmas*, vol. 18, no. 5, May 2011, Art. no. 053508, doi: 10.1063/1.3592990.

[6] A. J. Hatch and H. B. Williams, "The secondary electron resonance mechanism of low-pressure high-frequency gas breakdown," *J. Appl. Phys.*, vol. 25, no. 4, pp. 417–423, Apr. 1954, doi: 10.1063/1.1721656.

[7] A. J. Hatch and H. B. Williams, "Multipacting modes of high-frequency gaseous breakdown," *Phys. Rev.*, vol. 112, no. 3, pp. 681–685, Nov. 1958.

[8] D. H. Preist and R. C. Talcott, "On the heating of output windows of microwave tubes by electron bombardment," *IRE Trans. Electron Devices*, vol. 8, no. 4, pp. 243–251, Jul. 1961, doi: 10.1109/T-ED.1961.14797.

[9] J. R. M. Vaughan, "Some high-power window failures," *IRE Trans. Electron Devices*, vol. 8, no. 4, pp. 302–308, Jul. 1961, doi: 10.1109/T-ED.1961.14804.

[10] S. Yamaguchi, Y. Saito, S. Anami, and S. Michizono, "Trajectory simulation of multipactoring electrons in an S-band pillbox RF window," *IEEE Trans. Nucl. Sci.*, vol. 39, no. 2, pp. 278–282, Apr. 1992, doi: 10.1109/23.277497.

[11] P. Y. Wong, Y. Y. Lau, P. Zhang, N. Jordan, R. M. Gilgenbach, and J. Verboncoeur, "The effects of multipactor on the quality of a complex signal propagating in a transmission line," *Phys. Plasmas*, vol. 26, no. 11, Nov. 2019, Art. no. 112114, doi: 10.1063/1.5125408.

[12] N. Rozario, H. F. Lenzing, K. F. Reardon, M. S. Zarro, and C. G. Baran, "Investigation of telstar 4 spacecraft ku-band and C-band antenna components for multipactor breakdown," *IEEE Trans. Microw. Theory Techn.*, vol. 42, no. 4, pp. 558–564, Apr. 1994.

[13] *Special Sessions on Multipactor, I and II*, IEEE ICOPS, Denver, CO, USA, Jun. 2018.

[14] I. Montero, S. H. Mohamed, M. García, L. Galán, and D. Raboso, "Effect of surface reactions of low-energy carbon ions on the secondary electron emission of TiN:O thin films," *J. Appl. Phys.*, vol. 101, no. 11, Jun. 2007, Art. no. 113306, doi: 10.1063/1.2736861.

[15] A. Ruiz *et al.*, "UHV reactive evaporation growth of titanium nitride thin films, looking for multipactor effect suppression in space applications," *Vacuum*, vol. 81, nos. 11–12, pp. 1493–1497, Aug. 2007, doi: 10.1016/j.vacuum.2007.04.007.

[16] M. Ye *et al.*, "Suppression of secondary electron yield by microporous array structure," *J. Appl. Phys.*, vol. 113, no. 7, Feb. 2013, Art. no. 074904, doi: 10.1063/1.4792514.

[17] J. M. Sattler, R. A. Coutu, R. Lake, T. Laurvick, T. Back, and S. Fairchild, "Modeling micro-porous surfaces for secondary electron emission control to suppress multipactor," *J. Appl. Phys.*, vol. 122, no. 5, Aug. 2017, Art. no. 055304, doi: 10.1063/1.4997465.

[18] D. Wu *et al.*, "Fabrication of porous Ag/TiO_2/Au coatings with excellent multipactor suppression," *Sci. Rep.*, vol. 7, no. 1, p. 43749, Mar. 2017, doi: 10.1038/srep43749.

[19] A. Iqbal *et al.*, "Empirical modeling and Monte Carlo simulation of secondary electron yield reduction of laser drilled microporous gold surfaces," *J. Vac. Sci. Technol. B*, vol. 38, no. 1, 2020, Art. no. 013801, doi: 10.1116/1.5130683.

[20] C. Chang, G. Z. Liu, H. J. Huang, C. H. Chen, and J. Y. Fang, "Suppressing high-power microwave dielectric multipactor by the sawtooth surface," *Phys. Plasmas*, vol. 16, no. 8, Aug. 2009, Art. no. 083501, doi: 10.1063/1.3200900.

[21] O. A. Ivanov, M. A. Lobaev, V. A. Isaev, and A. L. Vikharev, "Suppressing and initiation of multipactor discharge on a dielectric by an external DC bias," *Phys. Rev. Special Topics-Accel. Beams*, vol. 13, no. 2, Feb. 2010, Art. no. 022004, doi: 10.1103/PhysRevSTAB.13.022004.

[22] A. Valfells, L. K. Ang, Y. Y. Lau, and R. M. Gilgenbach, "Effects of an external magnetic field, and of oblique radio-frequency electric fields on multipactor discharge on a dielectric," *Phys. Plasmas*, vol. 7, no. 2, pp. 750–757, Feb. 2000, doi: 10.1063/1.873861.
[23] A. Iqbal, J. Verboncoeur, and P. Zhang, "Multipactor susceptibility on a dielectric with two carrier frequencies," *Phys. Plasmas*, vol. 25, no. 4, Apr. 2018, Art. no. 043501, doi: 10.1063/1.5024365.
[24] V. Semenov, A. Kryazhev, D. Anderson, and M. Lisak, "Multipactor suppression in amplitude modulated radio frequency fields," *Phys. Plasmas*, vol. 8, no. 11, pp. 5034–5039, Nov. 2001, doi: 10.1063/1.1410980.
[25] S. Anza, C. Vicente, J. Gil, V. E. Boria, B. Gimeno, and D. Raboso, "Nonstationary statistical theory for multipactor," *Phys. Plasmas*, vol. 17, no. 6, Jun. 2010, Art. no. 062110, doi: 10.1063/1.3443128.
[26] S. Anza, C. Vicente, J. Gil, V. E. Boria, and D. Raboso, "Experimental verification of multipactor prediction methods in multicarrier systems," in *Proc. 46th Eur. Microw. Conf. (EuMC)*, Oct. 2016, pp. 226–229.
[27] S. A. Rice and J. P. Verboncoeur, "Migration of multipactor trajectories via higher-order mode perturbation," *IEEE Trans. Plasma Sci.*, vol. 45, no. 7, pp. 1739–1745, Jul. 2017, doi: 10.1109/TPS.2017.2704522.
[28] S. Lin, R. Wang, N. Xia, Y. Li, and C. Liu, "Stationary statistical theory of two-surface multipactor regarding all impacts for efficient threshold analysis," *Phys. Plasmas*, vol. 25, no. 1, Jan. 2018, Art. no. 013536, doi: 10.1063/1.5005042.
[29] V. E. Semenov *et al.*, "Simulations of multipactor thresholds in shielded microstrip lines," *J. Phys. D, Appl. Phys.*, vol. 42, no. 20, Sep. 2009, Art. no. 205204, doi: 10.1088/0022-3727/42/20/205204.
[30] A. A. Hubble, M. S. Feldman, P. T. Partridge, and R. Spektor, "Evolution of multipactor breakdown in multicarrier systems," *Phys. Plasmas*, vol. 26, no. 5, May 2019, Art. no. 053502, doi: 10.1063/1.5087069.
[31] R. Udiljak, D. Anderson, M. Lisak, V. E. Semenov, and J. Puech, "Multipactor in a coaxial transmission line. I. analytical study," *Phys. Plasmas*, vol. 14, no. 3, Mar. 2007, Art. no. 033508, doi: 10.1063/1.2710464.
[32] I. A. Kossyi *et al.*, "Experimental and numerical investigation of multipactor discharges in a coaxial waveguide," *J. Phys. D, Appl. Phys.*, vol. 43, no. 34, Aug. 2010, Art. no. 345206, doi: 10.1088/0022-3727/43/34/345206.
[33] Z. Fan *et al.*, "Experimental demonstration of improving resonant-multipactor threshold by three-dimensional wavy surface," *Appl. Phys. Lett.*, vol. 111, no. 12, Sep. 2017, Art. no. 123503, doi: 10.1063/1.5004131.
[34] C. Chang *et al.*, "The influence of desorption gas to high power microwave window multipactor," *Phys. Plasmas*, vol. 15, no. 9, Sep. 2008, Art. no. 093508, doi: 10.1063/1.2977988.
[35] K. D. Bergeron, "Theory of the secondary electron avalanche at electrically stressed insulator-vacuum interfaces," *J. Appl. Phys.*, vol. 48, no. 7, pp. 3073–3080, Jul. 1977, doi: 10.1063/1.324077.
[36] Y. Y. Lau, J. P. Verboncoeur, and A. Valfells, "Space-charge effects on multipactor on a dielectric," *IEEE Trans. Plasma Sci.*, vol. 28, no. 3, pp. 529–536, Jun. 2000.
[37] A. Iqbal, J. Verboncoeur, and P. Zhang, "Temporal multiparticle Monte Carlo simulation of dual frequency single surface multipactor," *Phys. Plasmas*, vol. 26, no. 2, Feb. 2019, Art. no. 024503, doi: 10.1063/1.5084143.
[38] D.-Q. Wen, A. Iqbal, P. Zhang, and J. P. Verboncoeur, "Suppression of single-surface multipactor discharges due to non-sinusoidal transverse electric field," *Phys. Plasmas*, vol. 26, no. 9, Sep. 2019, Art. no. 093503, doi: 10.1063/1.5111734.
[39] A. G. Sazontov and V. E. Nevchaev, "Effects of rf magnetic field and wave reflection on multipactor discharge on a dielectric," *Phys. Plasmas*, vol. 17, no. 3, Mar. 2010, Art. no. 033509, doi: 10.1063/1.3356082.
[40] A. A. Hubble, V. H. Chaplin, K. A. Clements, R. Spektor, P. T. Partridge, and T. P. Graves, "Multipactor breakdown threshold reduction due to magnetic confinement in parallel fields," *IEEE Trans. Plasma Sci.*, vol. 45, no. 7, pp. 1726–1730, Jul. 2017, doi: 10.1109/TPS.2017.2704923.
[41] D.-Q. Wen, P. Zhang, Y. Fu, J. Krek, and J. P. Verboncoeur, "Temporal single-surface multipactor dynamics under obliquely incident linearly polarized electric field," *Phys. Plasmas*, vol. 26, no. 12, Dec. 2019, Art. no. 123509, doi: 10.1063/1.5126438.
[42] H. C. Kim and J. P. Verboncoeur, "Transition of window breakdown from vacuum multipactor discharge to rf plasma," *Phys. Plasmas*, vol. 13, no. 12, Dec. 2006, Art. no. 123506, doi: 10.1063/1.2403782.
[43] H. C. Kim and J. P. Verboncoeur, "Time-dependent physics of a single-surface multipactor discharge," *Phys. Plasmas*, vol. 12, no. 12, Dec. 2005, Art. no. 123504, doi: 10.1063/1.2148963.
[44] A. Sazontov *et al.*, "Multipactor discharge on a dielectric surface: Statistical theory and simulation results," *Phys. Plasmas*, vol. 12, no. 9, Sep. 2005, Art. no. 093501, doi: 10.1063/1.2011348.
[45] M. Siddiqi and R. Kishek, "Construction of multipactor susceptibility diagrams from map-based theory," *IEEE Trans. Electron Devices*, vol. 66, no. 8, pp. 3587–3591, Aug. 2019, doi: 10.1109/TED.2019.2922147.
[46] M. Siddiqi and R. Kishek, "A predictive model for multipactor discharge in coaxial systems based on chaos theory," *IEEE Trans. Electron Devices*, vol. 66, no. 10, pp. 4403–4407, Oct. 2019, doi: 10.1109/TED.2019.2934457.
[47] W.-C. Tang and C. M. Kudsia, "Multipactor breakdown and passive intermodulation in microwave equipment for stellite applications," in *Proc. IEEE Conf. Mil. Commun.*, Oct. 1990, pp. 181–187, doi: 10.1109/MILCOM.1990.117409.
[48] L. Zhang *et al.*, "Numerical simulation and analysis of passive intermodulation caused by multipaction," *Phys. Plasmas*, vol. 25, no. 8, Aug. 2018, Art. no. 082301, doi: 10.1063/1.5027061.
[49] V. E. Semenov, E. I. Rakova, N. A. Zharova, J. Rasch, D. Anderson, and J. Puech, "Simple model of the rf noise generated by multipacting electrons," *J. Phys. D, Appl. Phys.*, vol. 47, no. 5, Jan. 2014, Art. no. 055206, doi: 10.1088/0022-3727/47/5/055206.
[50] A. Neuber, J. Dickens, D. Hemmert, H. Krompholz, L. L. Hatfield, and M. Kristiansen, "Window breakdown caused by high-power microwaves," *IEEE Trans. Plasma Sci.*, vol. 26, no. 3, pp. 296–303, Jun. 1998.
[51] J. R. M. Vaughan, "A new formula for secondary emission yield," *IEEE Trans. Electron Devices*, vol. 36, no. 9, pp. 1963–1967, Sep. 1989, doi: 10.1109/16.34278.
[52] J. R. M. Vaughan, "Secondary emission formulas," *IEEE Trans. Electron Devices*, vol. 40, no. 4, p. 830, Apr. 1993, doi: 10.1109/16.202798.
[53] P. Y. Wong, P. Zhang, and J. Verboncoeur, "Harmonic generation in multipactor discharges," *IEEE Trans. Plasma Sci.*, accepted, 2020.

Asif Iqbal (Student Member, IEEE) received the B.S. degree in electrical and electronic engineering from the Bangladesh University of Engineering and Technology, Dhaka, Bangladesh, in 2015. He is currently pursuing the graduate degree with the Electrical and Computer Engineering Department, Michigan State University, East Lansing, MI, USA.

His current research interest includes analytical and Monte Carlo modeling of multipactor and secondary electron emission.

Mr. Iqbal was a recipient of the Michigan Institute for Plasma Science and Engineering (MIPSE) Graduate Fellowship Award in 2019 and 2020, and the 2019 MIPSE Graduate Student Symposium Best Presentation Award.

Patrick Y. Wong (Member, IEEE) received the B.S.E., M.S.E., and Ph.D. degrees from the University of Michigan, Ann Arbor, MI, USA, in 2013, 2015, and 2018, respectively.

He is currently a Post-Doctoral Researcher with the Department of Electrical and Computer Engineering, Michigan State University, East Lansing, MI, USA. His research interests include theoretical and computational modeling of beam-circuit interactions in high power microwave devices including traveling-wave tubes, magnetrons, and multipactor.

John P. Verboncoeur (Fellow, IEEE) received the B.S. degree in engineering science from the University of Florida, Gainesville, FL, USA, in 1986, and the M.S. and Ph.D. degrees in nuclear engineering from the University of California at Berkeley (UCB), Berkeley, CA, USA, in 1987 and 1992, respectively.

He was a Post-Doctoral Researcher with the Lawrence Livermore National Laboratory, Livermore, CA, USA and also with the Department of Electrical Engineering and Computer Science (EECS), UCB. He was an Associate Research Engineer with the EECS, UCB, where he was a Nuclear Engineering Faculty in 2001 and a Full Professor in 2008. From 2001 to 2010, he served as the Chair with the Computational Engineering Science Program, UCB. In 2011, he joined Michigan State University (MSU), East Lansing, MI, USA, as a Professor of electrical and computer engineering and also a Professor of computational mathematics, science, and engineering, in 2015. He has authored or coauthored in MSU (formerly Berkeley) suite of particle-in-cell Monte Carlo codes, including XPDP1 and X-windows Object Oriented Particle-In-Cell code (XOOPIC), used by over 1000 researchers worldwide with over 350 journal publications in the last decade, 350 journal articles and conference papers, with over 3500 citations, and has taught 13 international workshops and minicourses on plasma simulation. His current research interests include theoretical and computational plasma physics, with a broad range of applications spanning low- temperature plasmas for lighting, thrusters, and materials processing to hot plasmas for fusion, from ultracold plasmas to particle accelerators, from beams to pulsed power, from intense kinetic nonequilibrium plasmas to high- power microwaves.

Dr. Verboncoeur was a Past-President of the IEEE Nuclear and Plasma Science Society and the IEEE Director-Elect. He was a recipient of the Department of Energy (DOE) Magnetic Fusion Energy Technology Fellowship. He is currently an Associate Editor of the *Physics of Plasmas*. He has served as a Guest Editor and/or a Frequent Reviewer for the IEEE TRANSACTIONS ON PLASMA SCIENCE, the IEEE TRANSACTIONS ON ELECTRON DEVICES, and as well as a number of other plasma and computational journals.

Peng Zhang (Senior Member, IEEE) received the B.Eng. and M.Eng. degrees in electrical and electronic engineering from Nanyang Technological University, Singapore, in 2006 and 2008, respectively, and the Ph.D. degree in nuclear engineering and radiological sciences from the University of Michigan (UM), Ann Arbor, MI, USA, in 2012.

He was an Assistant Research Scientist with the Department of Nuclear Engineering and Radiological Sciences, UM. He is currently Assistant Professor with the Department of Electrical and Computer Engineering, Michigan State University (MSU), East Lansing, MI, USA. He has authored refereed journal publications on electrical contacts, thin films, classical, ballistic, and quantum diodes, space-charge-limited current flows, beam-circuit interaction, multipactor and breakdown, microwave absorption on rough surfaces, slow wave structures, z-pinches, laser-plasma interaction, and more recently on vacuum nanodevices, quantum tunneling plasmonic junctions, ultrafast photoemission, and novel miniaturized electromagnetic radiation sources. His current research interests include theoretical and computational physics in nanoelectronics, plasmas, and accelerator technology.

Dr. Zhang was a recipient of the Air Force Office of Scientific Research (AFOSR) Young Investigator Program Award, the UM Richard and Eleanor Towner Prize for Outstanding Ph.D. Research, the UM Rackham Presidential Fellowship Award, and the IEEE Nuclear and Plasma Sciences Graduate Scholarship Award. He is currently serving as an Editorial Board Member for *Scientific Reports*, a Journal by Nature and Plasma Research Express, and a Journal by the Institute of Physics.